RSC Advances

ROYAL SOCIETY OF CHEMISTRY

www.rsc.org/advances

Up-converting HAP@β-TCP nanocomposite activated with Er^{3+}/Yb^{3+} ion-pairs for bio-related applications

Rafal J. Wiglusz[1*], Blazej Pozniak[2], Katarzyna Zawisza[1], and Robert Pazik[1]

[1]Institute of Low Temperature and Structure Research, Polish Academy of Sciences, P.O. Box 937, 50-937, Wroclaw, Poland

[2]Department of Biochemistry, Pharmacology and Toxicology, Faculty of Veterinary Medicine, Wroclaw University of Environmental and Life Sciences, 50-375 Wroclaw, ul. C.K. Norwida 31

Abstract

The HAP@β-TCP nanocomposites doped with Er^{3+}/Yb^{3+} ion-pairs were prepared using Pechini's technique. Structural properties and morphology of particles were studied by means of XRD, TEM, DLS techniques. Cytotoxicity of developed product was tested on canine osteosarcoma (D17) and murine macrophage (J774.E) cells. Determination of metronidazole release from HAP@β-TCP nanocomposite was done using dynamic dialysis and ultracentrifugation techniques. Thorough analysis of up-conversion properties of the prepared system was done showing that the GRR ratio depends strongly on the sample temperature induced by optical density of excitation and particle size. Relatively short decay times and behaviour of GRR ratio pointed out on the enhanced contribution of the non-radiative processes feeding the red emission.

Keywords: calcium hydroxyapatite, erbium, ytterbium, drug carrier, metronidazole release, nanoaprticle

[*]**Corresponding author:**

E-mail: R.Wiglusz@int.pan.wroc.pl;

Phone: +48-71-3954-159,

Fax: +48-71-344-10-29

1. Introduction

In recent years nanomaterials and nanocomposites have attracted wide interest due to their unusual mechanical, optical as well as magnetic properties[1,2]. Calcium phosphate compounds and their derivatives have been studied for biomedical applications because of their analogy to the inorganic component including organism systems[3,4]. Phosphate materials with the Ca/P ratio ~1.67 form different stable phases such as hydroxyapatite $Ca_{10}(PO_4)_6(OH)_2$ (HAP) and other phases such as tricalcium phosphate $Ca_3(PO_4)_2$ (α and β-TCP). It has been well known that HAP is bioactive and biocompatible with animal tissues, while the others are highly bio-resorbable[5]. Furthermore, these compounds display numerous advantages, such as bioactivity, biocompatibility that may be favorable for designing fluorescence bioprobes for bio-imaging and bio-sensing[6,7]. Although, the biomimetic properties of HAP were intensively studied for bone replacement and drug delivery, not much is known about the possibility to dope these materials with luminescent ions[8,9]. In order to control speed of biodegradation, a biphasic calcium phosphate (BCP) bioceramic containing both HAP and β-TCP are of significant interest[10]. Bioactivity and biodegradation of bioceramic containing both phases depends strongly on the ratio variation of HAP/β-TCP. The main difference is that β-TCP phase is more soluble and undergoes faster resorption than HAP allowing precipitation of apatites. In other words osteoconductivity is comparable among HAP and β-TCP.

Spectral properties of the apatites doped with rare earth cations like Nd^{3+}, Yb^{3+} or Er^{3+} ions have been studied[11,12,13]. However, the investigations were focused mostly on polycrystalline powders and single crystals, considering their applications as luminescent lamp phosphors and laser hosts. Due to local structural probing abilities of Eu^{3+} combined presence of hypersensitive transition, Eu^{3+} doped apatites have been studied relatively most frequently[14,15]. Most of bioapplications require nanosized materials but number of current studies on luminescent HAP nanoparticles is very limited. Highly efficient luminescent nanoparticles are attractive especially in the field of fluorescence imaging (FI). The most effective are the particles which are able to absorb in the NIR spectral region because most tissues generate little NIR fluorescence due to the weak NIR absorption and thus increase of the laser power does not cause any significant damages like in comparison high-energetic UV excitation. Additionally NIR has a deeper penetration depth than UV or VIS wavelengths and thus is not limited to only for shallow tissue imaging[16]. One of the promising alternatives lays in application of inorganic compounds such as mixed metal oxides or fluorides mutually co-

doped with optically active rare earth metals such as Yb^{3+}/Er^{3+} or Yb^{3+}/Tm^{3+} showing strong up-conversion[17]. The mechanism of this well known process relies on conversion of the incident infrared light to short wavelength emission in the visible range. The Yb^{3+} ions are considered as sensitizers which absorb the pumped light and then transfer absorbed energy directly to the activators such as Tm^{3+} or Er^{3+}. For the up-conversion process it is essential that the energy levels of sensitizer and activator are in resonance and this condition assures effective, efficient energy transfer and up-conversion fluorescence.

In the present study we demonstrate thorough studies of the HAP@β-TCP nanocomposite doped with up-converting Er^{3+}/Yb^{3+} ions focusing on nanoparticles cytotoxicity and anti-Stokes emission. Few possible implementation of prepared system in bio-related applications were discussed.

2. Experimental

2.1. Instruments

Development of crystalline phase was followed by means of XRD technique by collecting patterns in 2Θ range of 5–120° with X'Pert PRO X-ray diffractometer (Cu, Kα1: 1.54060 Å) (PANalytical). The microstructure and morphology of nanoparticles were investigated by high resolution transmission electron microscopy (HRTEM) using a Philips CM-20 Super Twin microscope, operated at 200 kV. Samples for measurements were prepared by making of dispersion of powders in methanol. Afterwards a droplet of suspension was deposited on a copper microscope grid covered with perforated carbon. The primary size of particles was evaluated using volume weighted formula:

$$d_{av} = \frac{\sum n_i d_i^4}{\sum n_i d_i^3}, \quad (1)$$

where d_{av} is the average particle size, n number of particles and d represents particle diameter. BET Specific surface area (SBET) was measured by nitrogen gas sorption at 77 K on a Quantachrome Autosorb IQ apparatus. Samples were degassed for 18 h at 100°C before starting. The particle size was calculated from BET measurements using following equation:

$$D_{BET} = \frac{6000}{dS_{BET}}, \quad (2)$$

where D_{BET} denotes an average particle size (nm), S_{BET} is the specific surface area (m^2/g) and d density of investigated material (g/cm^3). Hydrodynamic size was measured using dynamic light scattering technique with a Nanosight NS 500 automated instrument equipped with 405 nm line of laser diode as a light source backscattered further on measured objects. The

samples for hydrodynamic size measurements were prepared by taking 1 ml of water suspension containing nanoparticles and further on diluted with 19 ml of de-ionized water and transferred by peristaltic pumps to the sample chamber. Typically the starting concentration of nanoparticles in all prepared suspensions was around 1 mg/ml. Each measurement was repeated at least three times and conducted with different dilution of particles to achieve satisfactory statistics and exclude errors connected with too high or too low number of analyzed objects. From simultaneous measurement of the mean squared displacement of each particle tracked, the particle diffusion coefficient (D_t) and hence sphere-equivalent, hydrodynamic radius (r_h) can be determined using the Stokes-Einstein equation:

$$r_h = \frac{K_B T}{6\pi\eta D_t}, \quad (3)$$

where K_B is Boltzmann's constant, T is temperature and η is solvent viscosity (H_2O). The analysis was done using Nanosight NTA 2.3 software allowing for determination of particle/object concentration represented as a number of particles/objects per ml. The up-conversion luminescence spectra were recorded using Jobin Yvon THR 1000 monochromator equipped with a Hamamatsu R928 photomultiplier and a 1200 grooves/mm holographic grating. As an excitation source, continuous 975 nm line of 1.5 W laser diode was used. The luminescence decay times were measured utilizing a LeCroy Wave Surfer oscilloscope using pulsed 975 nm line of 10 mJ Ti:sapphire laser pumped by the 532 nm line of the YAG:Nd^{3+} laser. The power dependence of the up-conversion emission intensity I_{UPC} versus the excitation optical power I_{in} of 975 nm laser diode (CNI laser, China), were measured with a miniature fiber spectrometer (Avantes, Netherlands, spectral resolution ~3 nm) and fitted with an allometric dependence:

$$I_{UPC} = I_{in}^{N}, \quad (4)$$

to estimate the order of the up-conversion process N showing the number photons required to obtain anti-Stokes emission.

2.2. Synthesis of $Ca_{10}(PO_4)_6(OH)_2$@β-$Ca_3(PO_4)_2$:Er^{3+}/Yb^{3+} nanocomposites

The 2 mol% Er^{3+} and 10 mol% Yb^{3+} co-doped HAP@β-TCP nanocomposite powders were prepared by using 2.078 g (8.8 mmol) of $Ca(NO_3)_2 \cdot 4H_2O$ (99.995% Alfa Aesar), 0.03852 g (0.1 mmol) of Er_2O_3 (99.99% Alfa Aesar), 0.1970 g (0.5 mmol) of Yb_2O_3 (99.99% Alfa Aesar) and 0.7923 g (6 mmol) of $(NH_4)_2HPO_4$ (99.99% Alfa Aesar) utilizing modified Pechini's technique. Concentration of the rare earth cations (RE^{3+}) was set in respect to the overall molar content of Ca^{2+} cations. The stoichiometric amounts of RE^{3+} oxides were

initially digested in an excess of HNO_3 (ultrapure Avantor) in order to transform them into water soluble nitrates and eventually purified by triple recrystallization. Subsequently, calcium nitrate was dissolved in deionized water and mixed with erbium(III) and ytterbium(III) nitrates. Afterwards 24 g (0.125 mol) of citric acid (99.5% Sigma Aldrich) and 3.4 g (54.78 mmol) of ethylene glycol (ultrapure Avantor) were added under constant stirring at 60°C resulting in viscous mixture. Finally, $(NH_4)_2HPO_4$ was added and pH of solution containing all substrates was equilibrated with $NH_{3(aq)}$ (ultrapure Avantor) to achieve neutral pH. In fact, this step was repeated with additional pH settings (acidic and basic) in order to study the pH effect on the final composition of products. The turbid solution was obtained as a result of precipitation of by-products (amorphous phosphates). The mixture was further dried for 5 days at 90°C. The last step of synthesis involved post heat treatment at the temperature range of 800 – 1000°C for 3 hrs. The composition of the obtained samples was determined using inductively coupled plasma atomic emission spectrometry analysis (ICP-AES).

2.3. Determination of metronidazole release from HAP@β-TCP nanocomposite

Metronidazole (MTZ) loading and release from HAP@β-TCP nanocomposites (HAP@β-TCP_MTZ) was determined by means of high performance liquid chromatography (HPLC) with UV detection. To determine the total drug loading, 20 mg of powder was dissolved in 20 ml of 4% acetic acid and the resulting solution was analyzed for MTZ concentration. Calibration curve was prepared by spiking 4% acetic acid water solution with different concentrations of MTZ. The mean loading value (expressed in μg MTZ per mg of HAP@β-TCP) was calculated based on three independent experiments. Drug release was determined by the dynamic dialysis method and ultracentrifugation.

Dynamic dialysis

Twenty mg of powder was suspended in 5 ml of water, briefly vortexed and transferred into dialysis tubing (Spectrum Labs, 12 kDa MMWCO). The resulting dialysis chamber was immediately placed into a vessel with 50 ml of water (recipient fluid) and incubated at 37°C under constant and vigorous stirring. Sink conditions were maintained in the experiments, in that the concentration of MTZ in the recipient fluid at the end of the experiment did not exceed 10% of the initial drug concentration in the donor[18]. During the dialysis, 0.5 ml of the recipient fluid was sampled at following time points: 0; 1; 3; 5; 10; 20; 30; 45; 60; 90 and 120 min, and analysed for MTZ concentration. Each time the sampled volume was replaced with 0.5 ml of water. To ensure valid results, a control dialysis was performed in parallel. This was

prepared by spiking the pure HAP@β-TCP suspension with the appropriate amount of MTZ prior to standard dialysis procedure (as described above).

Ultracentrifugation method

Ten mg of powder was suspended in 50 ml of water and incubated for 120 min at 37°C under constant magnetic stirring. During the incubation, 0.3 ml of the suspension was sampled at following time points: 0; 1; 3; 5; 10; 20; 30; 45; 60; 90; 100; 110 and 120 min. The liquid was centrifuged (32 900×g, 5 min) and the supernatant analysed for MTZ concentration. After 90 min, 200 µl of acetic acid was added to dissolve the particles and release any possible drug residues (change of pH from 6.8 to 3.4).

HPLC determination of metronidazole

Metronidazole concentration was determined using a Waters Alliance® HPLC system with a Waters 2695 autosampler and Waters® 2996 Photodiode Array (PDA) detector set at 320 nm (Waters). A 150 × 2.1 mm i.d. reversed-phase column (PLRP-S 100A 5 µm, Agilent Technologies) with an appropriate guard column was used. The mobile phase comprised 90% 0.05 M CH_3COONH_4 at pH 4.3 and 10% acetonitrile (J.T. Baker). The flow rate was set at 0.1 mL/min. The limit of detection (LOD) was calculated by three times as the ratio of the standard deviation of the peak area in the time of elution to the slope (LOD = 3 × SD/slope) leading to the value of 2.6 ng/ml. The limit of quantification (LOQ), calculated by 10 times as the ratio of the standard deviation to the slope (LOQ = 10 × SD/slope) leading to the value of 8.8 ng/ml.

2.4. Cytotoxicity assessment of pure and metronidazole-loaded HAP@β-TCP nanoparticles in macrophage (J774.E) and osteaosarcoma (D17) cell lines

Cytotoxicity assessment was carried out on murine macrophage (J774.E) and canine osteosarcoma cell lines (D17). The choice of the J774.E cell line was based on the fact that under *in vivo* conditions, macrophages form the primary line of response to particulate matter. Thus they are responsible for the distribution and clearance of nanoparticles and their agglomerates. The second model (D17 cells) is a cancer cell line derived from the bone tissue which is rich in hydroxyapatites that play a fundamental role in the extracellular matrix formation. Cells were cultured in RPMI-1640 medium (Institute of Immunology and Experimental Therapy, Wrocław, Poland) supplemented with 10% fetal bovine serum (FBS, Sigma), L-glutamine (Sigma) and antibiotics (penicillin and streptomycin, Sigma). For the cytotoxicity assessment, cells were seeded in 96-well-plates (NUNC) at a density of 3×10^3 (D17) or 7×10^3 (J774.E) cells per well and pre-incubated at 37°C for 24 h in a humidified

atmosphere of 5% CO_2. After that, nanoparticle dispersions were added. Stock dispersions of pure HAP@β-TCP and HAP@β-TCP_MTZ were prepared based on a simplified version of the NANOGENOTOX dispersion protocol. Nanoparticles were suspended in 0.05% BSA water solution and bath-sonicated at room temperature for 1 min. Next, the stock dispersions were further diluted in 0.05% BSA and dispersed in complete culture medium. Cells were exposed to the HAP@β-TCP and HAP@β-TCP_MTZ dispersions for 48 h (5% CO_2, 37°C). After that, the MTT assay was carried out. The test is based on the enzymatic reduction of the tetrazolium salt MTT [3-(4,5-dimethylthiazol-2-yl)-2,5-diphenyl-tetrazoliumbromide] in living, metabolically active cells. The metabolite, purple-colored formazan was measured colorimetrically, using a multiwell plate reader. Preliminary experiment showed no interference of HAP@β-TCP or HAP@β-TCP_MTZ with either MTT or formazan in a cell-free system. After 2 h of incubation at 37°C, 80 µl of lysis buffer was added. The buffer consisted of 225 ml dimethylformamide (Sigma); 67.5 g sodium dodecyl sulphate (Sigma) and 275 ml distilled water. The optical density (OD) was measured after 24 hours using a spectrophotometric micro plate reader (ELx800, BioTek) at the wavelength of 570 nm (reference 630 nm). The OD of control cells was taken as 100%. Cell viability was determined as follows: % viability = (mean OD in the test wells/mean OD for control wells) × 100. The results were obtained from at least 3 independent experiments.

2.5. Preparation of $Ca_{10}(PO_4)_6(OH)_2$@β-$Ca_3(PO_4)_2$:Er^{3+}/Yb^{3+} lobes and pellets

The HAP@β-TCP lobes containing optically active ions were prepared directly from the freshly sintered and grinded nanocomposites using standard laboratory hydraulic press applying maximum 15 ton force on 0.1 g of powder during 60 seconds. As a result 1 mm thick lobes were obtained with diameter not exceeding 10 mm.

Spherical pellets containing HAP@β-TCP nanocomposites were prepared by vigorous mixing of 96 wg% of microcrystalline cellulose (Sigma Aldrich) and 4 wg% of HAP@β-TCP. After 60 sec, 77.5 ml of 20% water solution of polyvinylpyrrolidone (Sigma Aldrich) was added and mixing process was continued with three stop times desired for removal of scrape/wetted mass off the walls and bottom of container. The total mixing time was 5 min. Afterwards the mass was transferred into extruder operating at speed of 16 rpm and squeezed for 15 min. Subsequently, the extrudate was put into spheronizer for 10 min and at 800 rpm under flow of compressed air. The resulting pellets were sieved and two step drying process was applied, first at 35^0C for 5 h, and second in an ambient conditions for 48 h.

2.6. $Ca_{10}(PO_4)_6(OH)_2$@β-$Ca_3(PO_4)_2$:Er^{3+}/Yb^{3+} nanocomposite tooth root filling

Healthy moral tooth without cracks and signs of caries for root filling procedure was donated by REGMED Clinic, Poland from patient under orthodontic treatment. The tooth was thoroughly cleaned out of tissue debris and blood. In order to remove dental pulp cavity trepanation was performed using diamond dental bur mounted on handpiece. Subsequently, the cavity was rinsed with 4 ml of 5.25% NaClO (Chema-Elektromet, Poland) and distilled water. The tooth roots were adjusted to 18 mm in length and working distance was set at 0.5 mm short of the tooth apex. The root canals were explored with 15 mm K-file (Dentsply Maillefer, Switzerland), enlarged with 25 mm K-file (Dentsply Maillefer, Switzerland) as well as irrigated with 10 ml of 2% NaClO and 10 ml 0.9% NaCl after using each instrument. Afterwards, by using Lentulo spiral, roots and cavity were carefully filled with HAP@β-TCP paste and stored in incubator at 37^{o}C with 95% humidity for 3 days. Finally, the tooth was cut using microtome saw into two symmetrical samples.

2.7. $Ca_{10}(PO_4)_6(OH)_2$@β-$Ca_3(PO_4)_2$:Er^{3+}/Yb^{3+} nanocomposite deposition on implant

Basal osseointegrated type implant (BOI, IhdeDental, Germany) was covered with HAP@β-TCP layer using dip coating technique and further post annealing process. Beforehand BOI implant was washed out from possible impurities and fat using ultrasonic bath in acetone/ethanol mixture for 25 min and dryed at 40^{o}C for 1 h. In order to prepare dense water suspension of nanocomposite 10 g of HAP@β-TCP was taken and added into distilled water. Afterwards, the BOI was coated by dip-coating technique and carefully transferred to ceramic crucible for annealing at 450^{o}C for 3 h.

3. Results and discussion

Structural analysis of nanocomposite powders

It is well known that the β-TCP crystallizes in the rhombohedral space group *R3c* (see Figure 1a) having five different Ca^{2+} sites with coordination numbers 7 for Ca(1), 6 or 8 for Ca(2), 8 for Ca(3), 4 for Ca(4) (with partial cationic deficiency) and 6 for Ca(5) open for substitution with lanthanides[19]. On the other hand, the synthetic HAP adopts hexagonal structure depicted by the $P6_3$ space group (see Figure 1b) with two Ca^{2+} sites ninefold fold coordinated Ca(1) (C_3) and sevenfold coordinated Ca(2) (C_s) as well[20]. Since ionic radii of the Er^{3+} and Yb^{3+} cations are quite similar it can be predicted that these cations will enter most of

the Ca^{2+} sites in both compounds[21]. Therefore, as one would see, complex up-conversion emission spectra is anticipated.

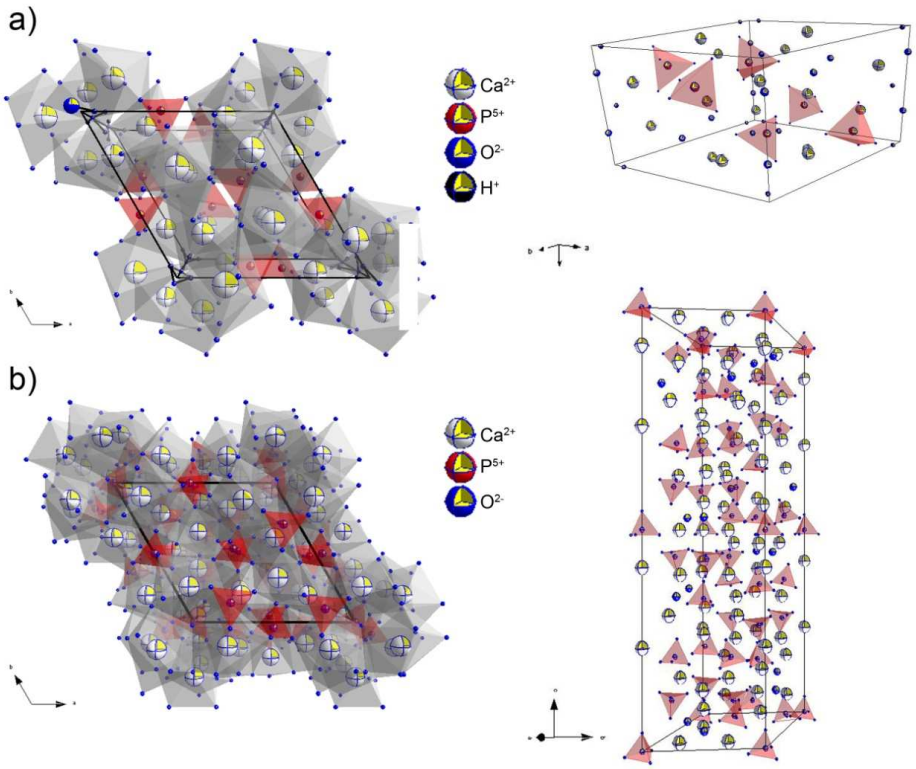

Fig. 1. The projections of crystal structure of (a) hexagonal $Ca_{10}(PO_4)_6(OH)_2$ hydroxyapatite with space group $P6_3$ (No. 173) and (b) trigonal $Ca_3(PO_4)_2$ with space group R3c (No. 161)

Fabrication process of the HAP@β-TCP nanocomposites doped with Er^{3+} and Yb^{3+} was divided into two crucial steps. The former one involved reaction pH testing since formation of separate β-TCP and HAP phases is driven by this parameter. Once proper pH was found, the main aim of the latter step was to study the optimal post temperature treatment to find a balance between sufficient crystallinity, particle size and phase content relation. As it can be seen (see Figure 2) the synthesis carried out at acidic pH leads directly to formation of only the β-TCP phase whereas neutral reaction condition results in a mixture of the HAP and β-TCP. At basic pH only the HAP phase could be detected. Therefore, the effect of annealing temperature on crystal structure and phase content was studied for samples prepared at neutral pH.

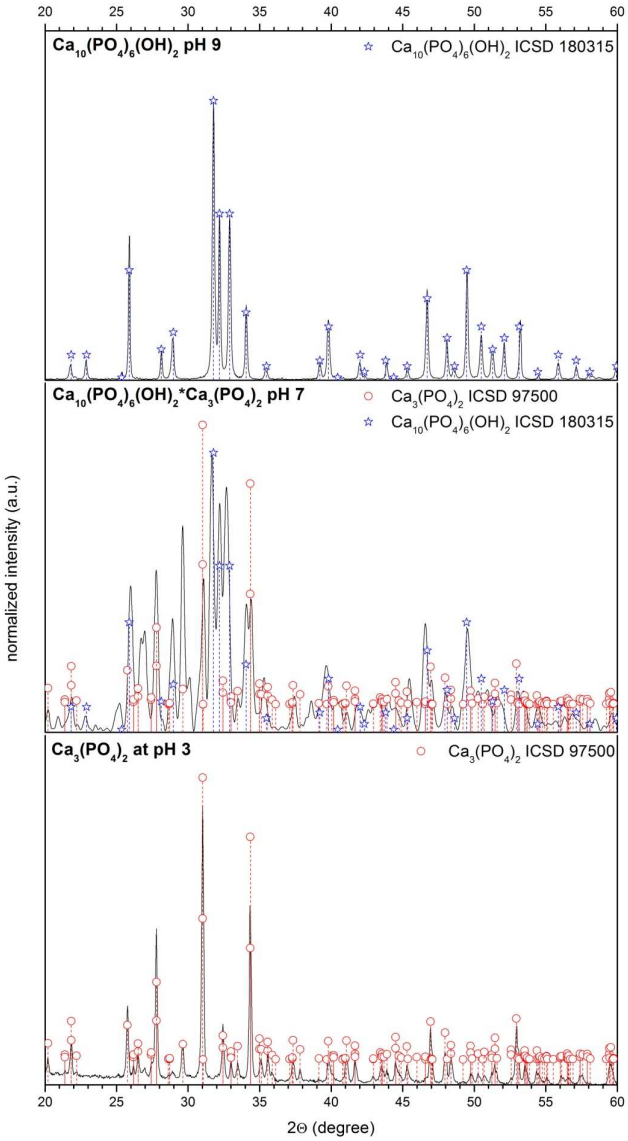

Fig. 2. The pH effect on formation of the β-TCP, HAP@β-TCP and HAP formation.

The structure evolution of the HAP@β-TCP nanocomposites doped with Er^{3+} and Yb^{3+} cations was followed by XRD technique as a function of annealing temperature in the range of 800 - 1000°C (Figure 3). This specific temperature regime was dictated by several factors. Firstly, it was necessary to start sintering from 800°C since below that temperature significant amount of residual carbon content under specific treatment condition would be present. One could overcome this problem by extending time of annealing process. However, a drawback was seen in unwanted growth of particles. Secondly, it is well known that above 1000°C β-TCP transforms into high temperature α-TCP phase. This means that fabrication of nano α-TCP is questionable at such temperature[22]. Additionally, the rate of resorption of α-TCP is too quick for biological applications[23] thus presence of α-TCP would be treated as an unwanted impurity as well.

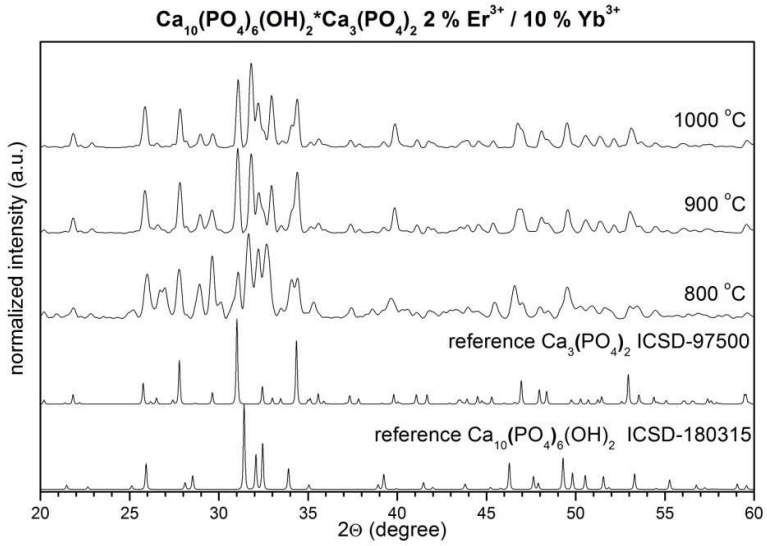

Fig 3. Effect of the annealing temperature on the structure evolution of the HAP@β-TCP nanocomposite.

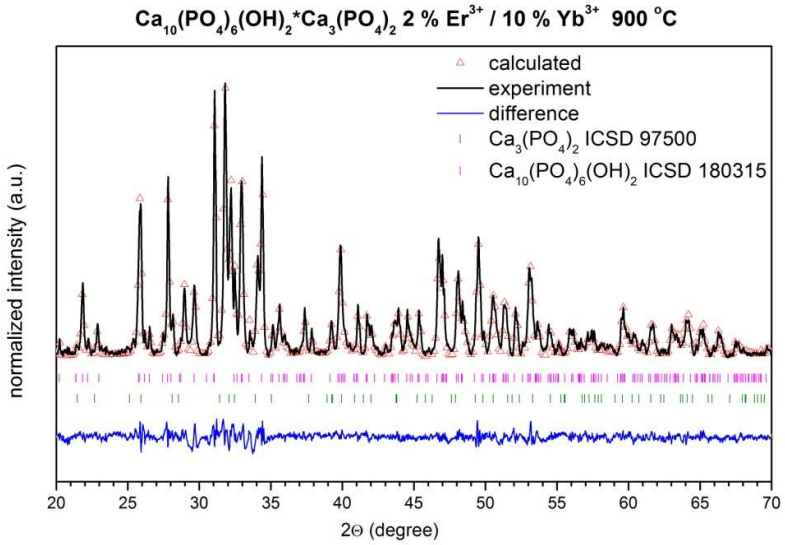

Fig. 4. Representative result of the Rietveld analysis of the HAP@β-TCP doped with 2% Er^{3+} /10% Yb^{3+} heated at 900°C (XRD pattern - black lines, red - fitted diffraction; blue - differential pattern; column - reference phase peaks position).

Thorough structural analysis (Figure 4) was done basing on the Rietveld method[24]) incorporating anisotropic approach[25,26] in Maud 2.33 software[27]. Fitting results were gathered in table I. In both cases annealing temperature shows no clear dependence on the structural properties of HAP and β-TCP. However, it is interesting to note that for the nanocomposite sintered at 800°C unit cell parameters were significantly different. For instance cell volume of the HAP phase was relatively large. It contracts above 900°C and remained almost unchanged at 1000°C. Reverse behavior was seen in case of the second β-TCP phase where cell volume expands upon 900°C having the smallest value at 800°C. It was quite complicated to fully comprehend this effect, but unit cell contraction would be definitely connected with

substitution of the large cations Ca^{2+} with smaller Er^{3+} and Yb^{3+} cations for both phases (compare with reference data). Additionally, expansion of the cell volume in case of the HAP phase might be seen in so-called size effect where action of negative pressure on the crystal lattice for small particles could lead to such results[28]. Thus, it could also mean that the size of the HAP nanoparticles is smaller than β-TCP phase or this effect is stronger reflected by the HAP. It was worth noting that the both phase content relation changes from 45 % of HAP and 54 % of β-TCP at 800°C for almost 60 % of HAP and 40% of β-TCP above this temperature. It is well known that sintering of HAP at elevated temperature could lead to the dehydration, dehydroxylation and finally decomposition of the HAP. This process could be reversible upon material contact with humidity unless more stable phases are formed (β and/or α-TCP). Therefore, one could expect increase of the β-TCP phase content with temperature. However, since the XRD measurement of samples heated above 800°C was done after cooling down than the interplay of both phases is similar since water absorption might occur leading to the hydration β-TCP and formation of the HAP.

Table. I. Unit cell parameters (a and c), crystal cell volume (V), as well as refined factor (R_w) for the HAP@β-TCP nanocomposite doped with 2% Er^{3+} / 10% Yb^{3+}as a function of sintering temperature.

Sample	Cell parameters						Phase		
	HAP			β-TCP			HAP	β-CP	
	a (Å)	*c* (Å)	*V* (Å^3)	*a* (Å)	*c* (Å)	*V* (Å^3)	(%)	(%)	R_{wp} (%)
s. c.*	9.5500	6.8700	542.62	10.4352(2)	37.4029(5)	3527.26	–	–	–
800°C	9.5290(6)	6.8445(1)	538.23(6)	10.4264(8)	37.3453(0)	3515.94(4)	45	54	3.20
900°C	9.4255(7)	6.8853(0)	529.74(7)	10.4354(2)	37.3885(5)	3526.05(5)	58	42	2.52
1000°C	9.4287(7)	6.8812(1)	529.79(2)	10.4367(1)	37.3914(9)	3527.20(4)	59	41	3.50

*s.c. - single crystal reference data, HAP - ICSD 180315, β-TCP - ICSD 97500

Evaluation of primary particle size and shape of the HAP@β-TCP was done by means of TEM microscopy (Figure 5) whereas DLS technique was employed in order to extract hydrodynamic size of objects present in water suspension (Figure 6). Both techniques are of great importance in characterization of nanoobjects but in the most cases could lead to different results. The main issue here was as follows TEM gives only information regarding primary size of particles and is performed on dry powders. Even though, the final material shown presence of fairly large agglomerates of particles. It was quite easy to recognize single particles and estimate their size and distribution. However, in the most cases some authors are not troubled about presence of agglomerates and give only the average particle size. This is actually critical for biological applications. Thus, in order to study behavior of particles in water or biological media it is more important to answer on the question how the state of particles is affected by the different type of solvents and additives used for preparation of

suspensions or colloids. Therefore, the DLS technique steps into the light as the method providing more adequate or realistic results regarding the size of all objects present in the colloid.

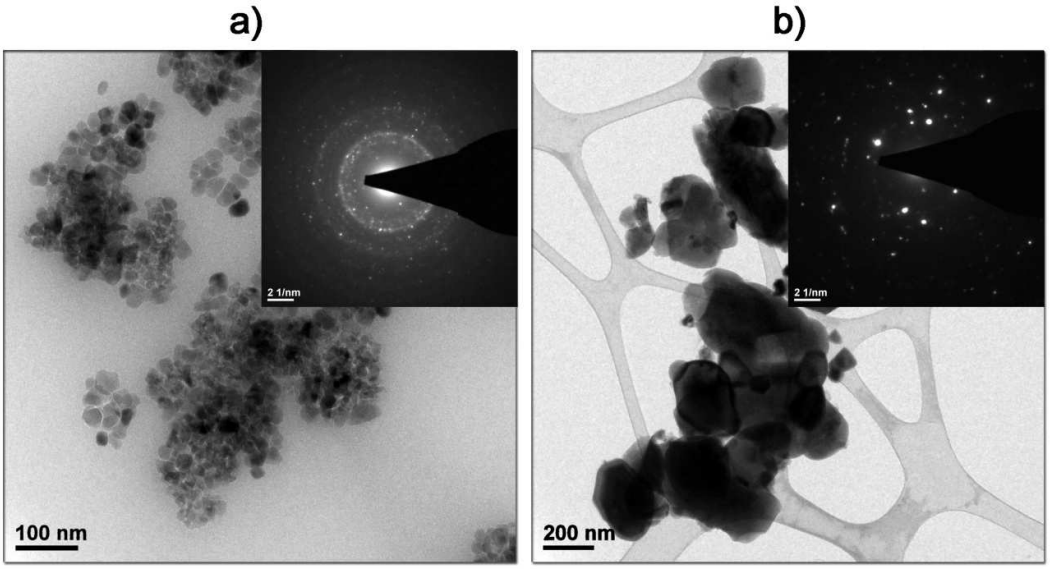

Fig. 5. TEM and SAED images of selected HAP@β-TCP composites prepared at 800°C (a) and 1000°C (b) doped with 2 mol% Er^{3+} and 10 mol% Yb^{3+} ions.

In accordance with the TEM analysis the HAP@β-TCP nanocomposite sample annealed at 800^{o}C contains loosely agglomerated irregular particles with primary size of 22 nm which were starting to grow rapidly above 200 nm at 1000^{o}C. Since, the aim of the studies was to obtain nanocomposites further characterization was performed on samples heat treated at 800^{o}C.

In order to prepare stable colloidal solution of the HAP@β-TCP nanocomposite adenosine 5'- tetrahydrogen triphosphate (ATP) was added as a stabilizing agent preventing the system against progressing in time agglomeration[29]. The hydrodynamic size was measured 24 and 48 h after modification of HAP@β-TCP with ATP showing comparable values of 220 nm (Figure 6). As one can see this result goes well with TEM analysis but only after taking into account the size of agglomerates visible in Figure 5a.

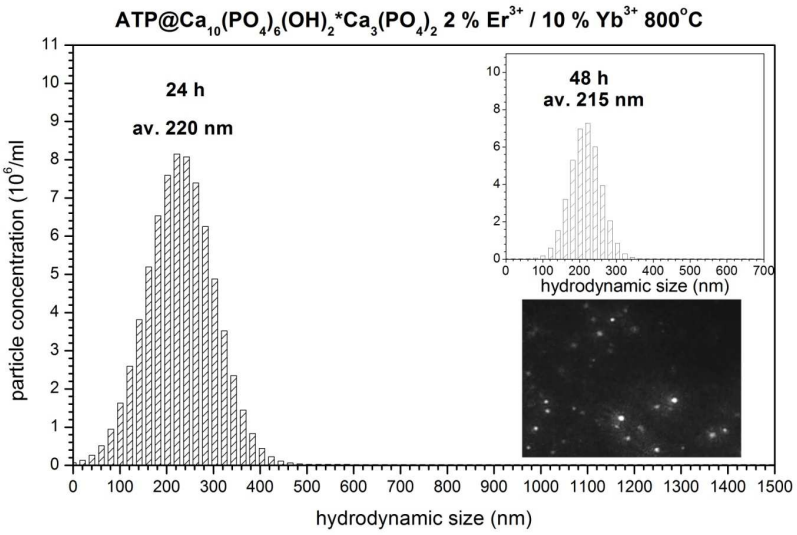

Fig. 6. Hydrodynamic size of selected $Ca_{10}(PO_4)_6(OH)_2 \cdot Ca_3(PO_4)_2$ composite prepared at 800°C doped with 2 mol% Er^{3+} and 10 mol% Yb^{3+} ions modified by ATP - adenosine 5'- tetrahydrogen triphosphate.

Actually, this was a nice proof of the simple fact that once dry non-blocked by surface agents nanoparticles were transferred into water based suspension the size estimated by these two techniques could be completely different[30]. Finally, the grain size of the HAP@β-TCP nanocomposite sintered at 800°C was verified after measuring the surface area of this sample (24 m^2/g) leading to the value of 79.36 nm. For the calculation sample density was taken from the Rietveld refinement being 3.14 g/cm^3. Both, the TEM and BET analysis confirmed nano-sized character of the HAP@β-TCP sample heated at 800°C.

Metronidazole release and cytotoxicity of nanocomposites

Many inorganic nanomaterials can serve as carriers of drugs or other biologically important substances showing prospects in biomedicine applications[31]. Therefore, the nanocomposite of HAP@β-TCP doped with 2 mol% of Er^{3+} and 10 mol% of Yb^{3+} was loaded with the metronidazole (antibiotic used against anaerobic bacteria) according to the given protocol. Drug loading of HAP@β-TCP_MTZ was found to be 9.89 μg/mg of powder. Results of the MTZ release from the HAP@β-TCP by means of dynamic dialysis were summarized in Figure 7.

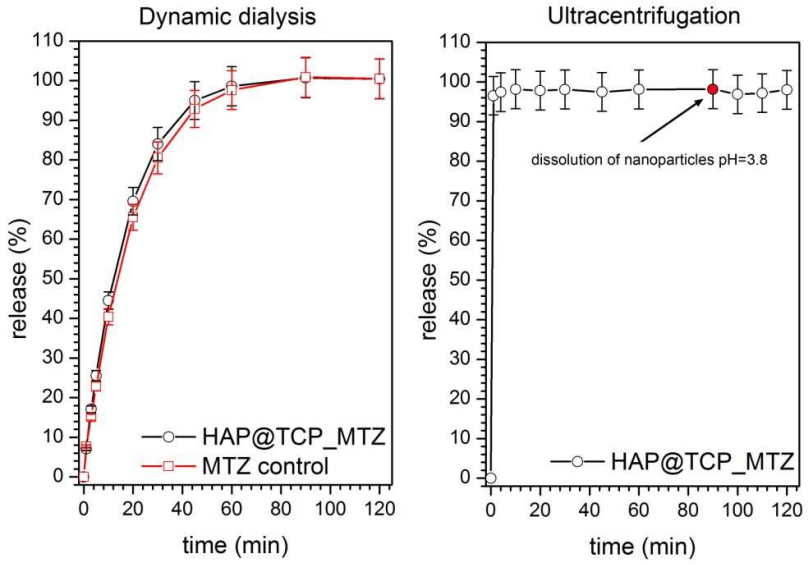

Fig. 7. Release of the metronidazole from HAP@β-TCP nanocomposite by dynamic dialysis (left) and ultracentrifugation methods (right).

A rapid increase of MTZ concentration in the recipient fluid has been observed during the initial 60 min of the dialysis. After this period, a plateau was reached indicating the equilibrium between the drug concentration in the donor and the recipient. The kinetics of this increase was almost identical for the drug-loaded nanoparticles and blank HAP@β-TCP suspension spiked with MTZ. This indicates that the increase of the drug's concentration was entirely governed by its permeation through the cellulose membrane and possible secondary interactions with suspended particles. Moreover, another conclusion might be drawn regarding weak or even lack of binding between the particles and the drug which was even better visualised in Figure 7. In the ultracentrifugation method, there is no barrier (i.e. dialysis membrane) that would delay the free drug molecules from entering the liquid surrounding the particles. In the present study, nearly 100% of the drug was present in the liquid instantly after HAP@β-TCP_MTZ particle were dispersed. It confirms the lack of drug binding observed earlier with the dynamic dialysis method. Dissolution of particles after 90 min of incubation did not change MTZ level in the solution. This excludes the presence of MTZ residues in the particle agglomerates. Thus, the HAP@β-TCP_MTZ system might be used for instance as bifunctional material working in the same time as an immediate drug releasing carrier in hydrophilic biological media stimulating treatment of the bacterial infections in dental/jaw surgery and regenerative material in bone surgery.

The effects of HAP@β-TCP and HAP@β-TCP_MTZ on cell viability are summarized in Figure 8. No significant effect of either HAP@β-TCP or HAP@β-TCP _MTZ on J774.E cells viability was observed, even at the highest concentration of 100 µg/ml. In the case of D17

cells the response was more variable. Metronidazole-loaded nanoparticles showed a relatively slight dose-dependent decrease in cell viability whereas pure HAP@β-TCP did not induce any significant effect. Antiproliferative effects of pure hydroxyapatite nanoparticles towards different cancer cell lines were described by several authors[32,33]. In the present study, pure HAP@β-TCP did not show cytotoxicity but it cannot be excluded that loading the particles with the chemotherapeutic may have triggered the cytotoxic effect due to unknown mechanism. On the other hand, the decrease in cell viability did not reach 50% even at the highest nanoparticle concentration. Considering this, it may be concluded that neither HAP@β-TCP nor HAP@β-TCP _MTZ show significant cytotoxicity in the studied cell lines.

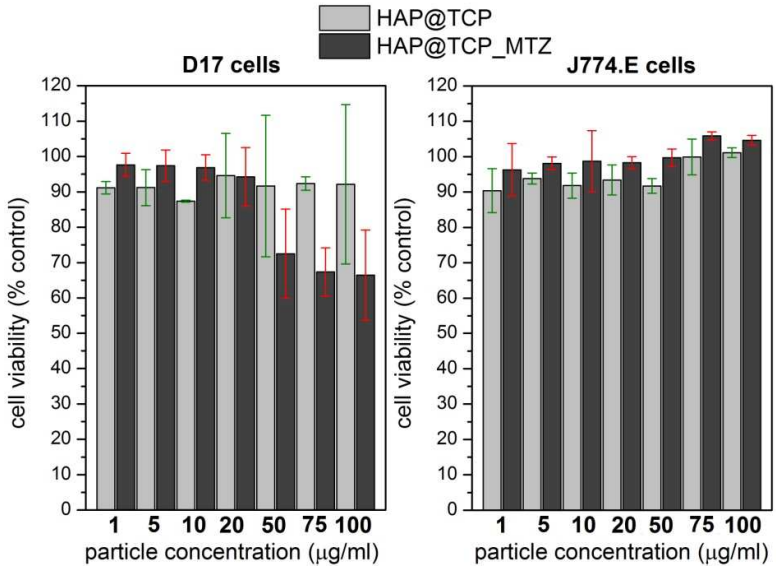

Fig. 8. Mean (±SD) viability of D17 canine osteosarcoma cells (left) and J774.E murine macrophages (right) exposed for 48 h to different concentration of pure HAP@β-TCP and nanoparticles loaded with metronidazole (HAP@β-TCP_MTZ). Viability expressed as the percent of control (results obtained from 3 independent experiments).

Optical properties

The absorption reflectance spectra of the HAP@β-TCP sample containing 2 mol% of Er^{3+} and 10 mol% of Yb^{3+} ions heated at 800°C was measured at 300 K in order to reveal some characteristic spectral features of both co-dopants (see Figure 9). The spectra consists of typical absorption bands covering the UV and NIR regions associated with the intra-configurational *f-f* electron transition of both ions. Thus, the group of lines with sharp maxima at 379 nm (26 385 cm^{-1}) was attributed to the $^4I_{15/2} \rightarrow {}^4G_{11/2}$ electron transition, at 488.9 nm (20 454 cm^{-1}) to the $^4I_{15/2} \rightarrow {}^4F_{7/2}$, at 521.9 nm (19 160 cm^{-1}) to the $^4I_{15/2} \rightarrow {}^2H_{11/2}$, as well as 1433.02 (6978 cm^{-1}) to the $^4I_{15/2} \rightarrow {}^4I_{13/2}$ all of them belonging to the Er^{3+} ions. The

characteristic band with maxima at 981 nm (10 193 cm^{-1}) was ascribed to the $^2F_{7/2} \rightarrow {}^2F_{5/2}$ absorption transition of Yb^{3+} ions which additionally could hinder the $^4I_{15/2} \rightarrow {}^4I_{11/2}$ absorption transition of the Er^{3+}. It has to be stressed out that the intensities of all recorded bands are comparable. It is expected that this behaviour will have striking consequences in identification of the exact up-conversion mechanism ETU or ESA. It is well known that the absorption cross section of Yb^{3+} (the $^4F_{7/2}$ level) at 975 nm is much higher than Er^{3+} (the $^4I_{11/2}$ level). Therefore, use of additional strongly absorbing resonant co-dopants such as Yb^{3+} will significantly promote the efficiency of energy transfer to the activator (Er^{3+})[34].

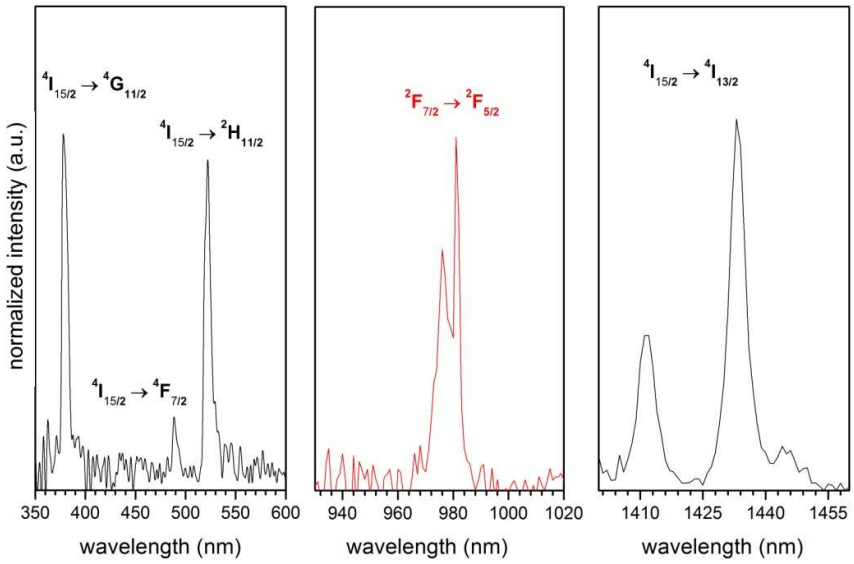

Fig. 9. Absorption reflectance spectra of the $Ca_{10}(PO_4)_6(OH)_2{\cdot}Ca_3(PO_4)_2$ composite doped with 2 mol% Er^{3+} and 10 mol% Yb^{3+} ions prepared at 800°C.

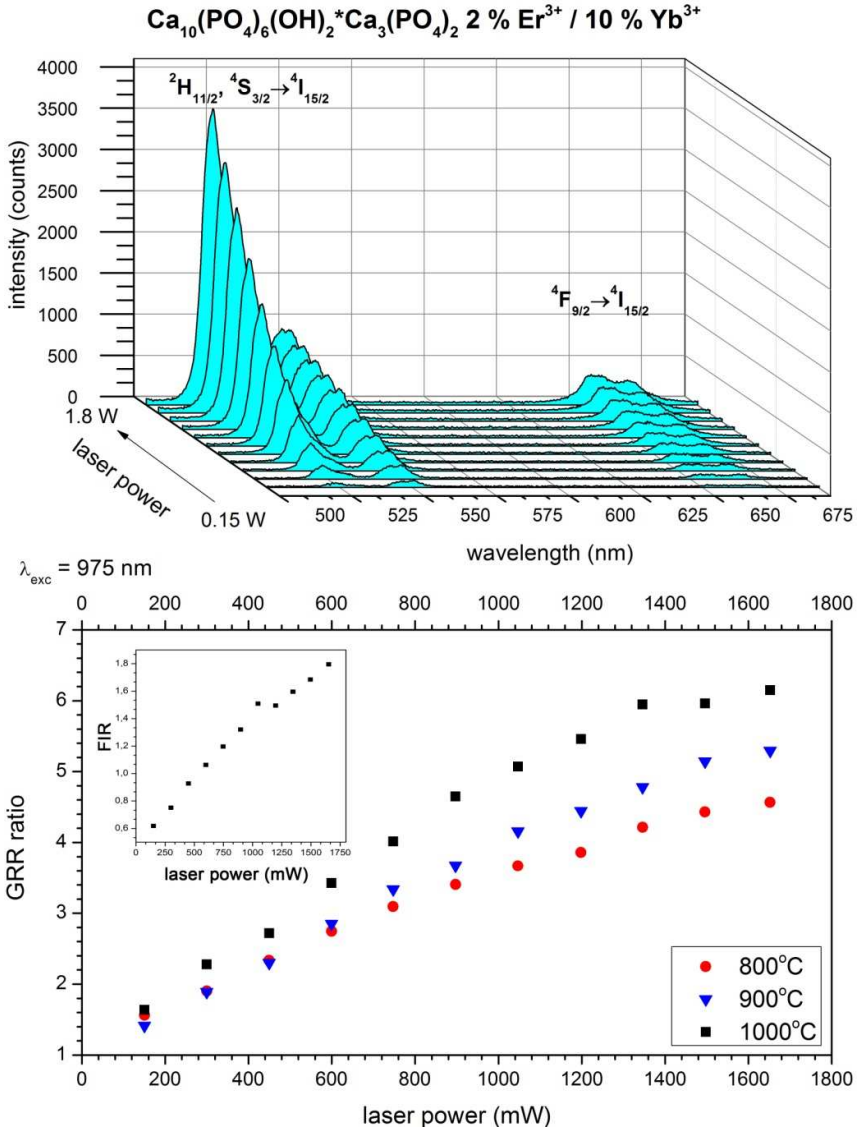

Fig. 10. Up-conversion emission spectra as function of laser power (upper) GRR ratio (bottom) together with FIR power dependence (inset) of the $Ca_{10}(PO_4)_6(OH)_2 \cdot Ca_3(PO_4)_2$ composite doped with 2 mol% Er^{3+} and 10 mol% Yb^{3+} ions prepared at 800°C.

The up-conversion emission spectra of the HAP@β-TCP sample containing 2 mol% of Er^{3+} and 10 mol% of Yb^{3+} ions thermally treated at 800°C measured at 300 K were recorded after direct excitation at 975 nm under different laser power regimes (Figure 10). Typical anti-Stokes emission transitions can be individuated as group of lines in the green spectral range of 505 - 575 nm (19 801 - 17 391 cm^{-1}) ascribed to the $^2H_{11/2}, ^4S_{3/2} \rightarrow {}^4I_{15/2}$ electron transitions and covering red region of 635 - 689 nm (15 748 - 14 513 cm^{-1}) attributed to the $^4F_{9/2} \rightarrow {}^4I_{15/2}$ electron transition. One can note that the emission spectra are relatively broad and peaks are not resolved into specific Stark components. The most likely for the broadening of the emission lines existence of different crystallographic sites occupied by Er^{3+} and Yb^{3+} ions in

both HAP and β-TCP structures was the main feature responsible since all of the Er^{3+} were excited in the same time resulting in spectral overlap of the emission lines. Another contribution could be sought in presence of structural defects induced by doping with cations with different oxidation states (charge compensation effect) and/or their heterogeneous distribution due to the increased surface to volume ratio in nanomaterials. Moreover, it was worth to mention that the intensity interplay between two green transitions of the $^2H_{11/2} \rightarrow {}^4I_{15/2}$ and the $^4S_{3/2} \rightarrow {}^4I_{15/2}$ changed drastically upon of the laser power in favour of former one. The reason is quite simple and well written in the literature but has great practical implications especially in the field of temperature sensing[35]. Actually the Er^{3+} is one of the best candidates for realization of such purpose since this particular ion has appropriate structure of energy levels (see Figure 11). It well known that if considered levels are relatively close to each other, as in the case of the $^2H_{11/2}$ and $^4S_{3/2}$ in Er^{3+}. Their population represented as the integrated fluorescence intensity ratio (FIR) is driven by the Boltzmann's distribution in the following manner:

$$FIR = \frac{I(^2H_{11/2} \rightarrow {}^4I_{15/2})}{I(^4S_{3/2} \rightarrow {}^4I_{15/2})} = \frac{g_H A_H h\nu_H}{g_S A_S h\nu_S} \exp(-\frac{\Delta E}{kT}) = B\exp(-\frac{\Delta E}{kT}) \quad (5),$$

where g_H and g_s are the degeneracy of the $^2H_{11/2}$ and $^4S_{3/2}$ levels, A_H, A_S and ν_H, ν_S are the spontaneous emission rates and frequencies of the $^2H_{11/2} \rightarrow {}^4I_{15/2}$ and the $^4S_{3/2} \rightarrow {}^4I_{15/2}$ transitions, h is the Planck's constant, k is the Boltzmann's constant, T is absolute temperature and ΔE is energy gap[36]. After transformation of the equation (5) into linear dependence:

$$\ln(FIR) = \ln(B) + (-\frac{\Delta E}{kT}) = \ln(B) + (-\frac{C}{T}), \quad (6)$$

B and C constants can be extracted. The energy gap ΔE equals to 810 cm^{-1} meaning that the C constant is 1165 cm^{-1} (k = 0.6952 $K^{-1}cm^{-1}$). Assuming that the sample has 300 K *FIR* can be obtained by extrapolation of power dependence of *FIR* giving value of 0.57 at zero limit of laser power (see inset in Figure 10)[37]. Therefore taking into account equation (6) *ln(B)* is 3.32. Thus for the highest optical laser power of 1.65 W (52.52 W/cm^2) and *FIR* = 1.79 T is 425 K.

It was interesting to note that the intensity of the green part of spectra strongly increased over red region with increase of laser power as well. Analysis of the integrated intensity ratio between green transitions and red one could be treated as indirect method for estimation of efficiency of the up-conversion process (green-to-red ratio GRR)[38]. The general rule is as follows, if the red band intensity increases at the expense of green bands than efficiency of the up-conversion process decreases due to the enhanced role of the non-radiative processes (cross-relaxation, multiphonon relaxation). Therefore, the higher the GRR value the better

performance of up-converting system. This simple method could be the base for comparison of the different materials. The GRR ratio is expected to be dependent on the type of phase in terms of symmetry of occupied sites, since the closest surrounding influence the splitting in crystal field as well as depends on excitation power inducing thermal effects influencing directly population of electronic states[39]. One can clearly see (Figure 10 right) that the GRR ratio of the HAP@β-TCP 2 mol% of Er^{3+} and 10 mol% of Yb^{3+} nanocomposite strongly increased upon laser power from low power regime of 5.7 W/cm^2 (0.18 W) GRR is 1.4 up to 6.2 for 57.3 W/cm^2 (1.8 W). This change was definitely caused by the sample self heating and thermalization process resulting in higher population of the $^2H_{11/2} \rightarrow {}^4I_{15/2}$. It has to be emphasised that GRR depends also on the grain size of particles. The highest values were achieved for the largest particles since the smaller ones contain higher fraction of optically active cations located closer to the surface which were prone for non-radiative deactivation (impurities, surface states, defects etc.).

In the case of the up-conversion emission three main mechanism were proposed APTE effect (for addition de photon par transfer d'energie) named also as ETU (energy transfer up-conversion, excited state absorption (ESA) and photon avalanche (PA)[40]. In majority of cases ETU and ESA were the most effective. However, due to the quadratic power dependence it was difficult to differentiate them. Schematic energy-level diagram presenting the mechanism of up-conversion and accompanying processes was shown in Figure 11. After absorption of NIR photons by both Yb^{3+} and Er^{3+} electrons from the ground states $^2F_{7/2}$ and $^4I_{15/2}$ were excited to the $^2F_{5/2}$ and $^4I_{11/2}$ levels by GSA process instantaneously. Additional incoming photon moved electrons from $^4I_{11/2}$ level to the $^4F_{7/2}$ by excited state absorption (ESA).

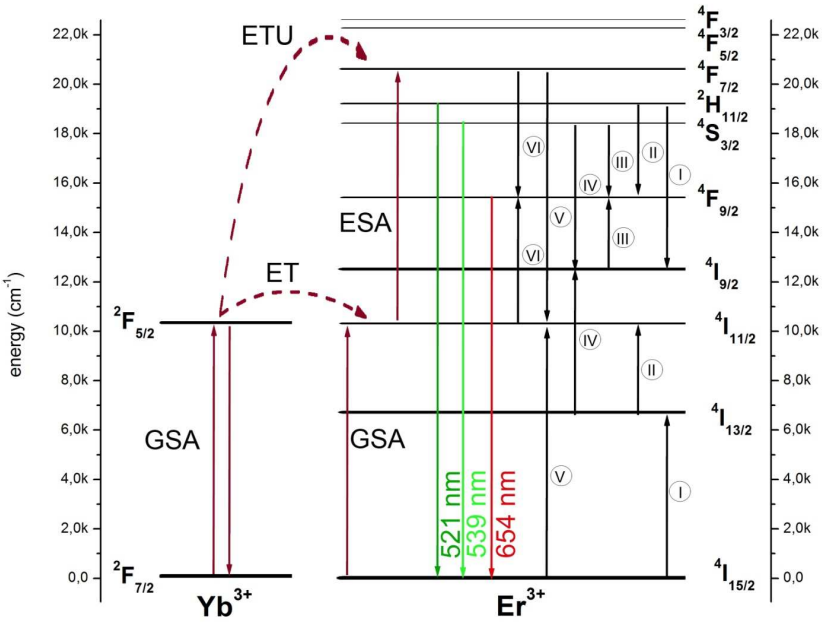

Fig. 11. Simplified energy level scheme presenting up-conversion and CR processes.

Due to the large absorption cross section of Yb^{3+} ions majority of the excitation energy was absorbed by Yb^{3+} and electrons at the $^2F_{5/2}$ could be directly transferred to the $^4I_{11/2}$ level of the Er^{3+} by ET (energy transfer) and/or to the $^4F_{7/2}$ level of Er^{3+} by ETU (energy transfer up-conversion) process. Both processes ETU and ESA demand participation of two photons. Afterwards, electrons from the $^4F_{7/2}$ level relaxed very fast non-radiatively to the $^2H_{11/2}$ and $^4S_{3/2}$ levels via multiphonon relaxation process (MPR). From these levels radiative de-excitation could occur to the $^4I_{15/2}$ resulting in green emission eventually. Since, there is always competition between radiative and non-radiative depopulation part of electrons could be lost on feeding of $^4F_{9/2}$ level due to the multiphonon relaxation process of the $^2H_{11/2} + {}^4S_{3/2}$ levels or cross relaxation (CR). This behaviour could be tuned by careful selection of host lattice, balance of co-dopants concentration, grain size and synthetic parameters. The CR is strongly concentration and laser-power sensitive. One can individuate following several highly probable CR processes:

$$(^2H_{11/2} + {}^4S_{3/2}, {}^4I_{15/2}) \rightarrow (^4I_{9/2}, {}^4I_{13/2}) \quad \text{(I)}$$

$$(^2H_{11/2} + {}^4S_{3/2}, {}^4I_{13/2}) \rightarrow (^4F_{9/2}, {}^4I_{11/2}) \quad \text{(II)}$$

$$(^4S_{3/2}, {}^4I_{9/2}) \rightarrow (^4F_{9/2}, {}^4F_{9/2}) \quad \text{(III)}$$

$$(^4S_{3/2}, {}^4I_{13/2}) \rightarrow (^4I_{9/2}, {}^4I_{9/2}) \quad \text{(IV)}$$

$$(^4I_{11/2}, {}^4I_{11/2}) \rightarrow (^4I_{15/2}, {}^4F_{7/2}) \quad \text{(V)}$$

$$(^4I_{11/2}, {}^4F_{7/2}) \rightarrow (^4F_{9/2}, {}^4F_{9/2}) \qquad \text{(VI)}$$

all of them contributing to decrease of the green emission and GRR ratio. Additionally, since the energy gaps of the $^4S_{3/2}$ and $^4F_{9/2}$ as well as $^4F_{9/2}$ and $^4I_{9/2}$ levels equal to 3 000 and 2 850 cm^{-1} respectively, the emission may be effectively quenched by phonons from vibrations of the ν_4 PO_4^{3-} and ν_3 PO_4^{3-} phosphate groups or surface defects like OH^- bridging the energy mismatch. This behavior, may also suggest, that ESA dominates over ETU, which would be also confirmed by less efficient up-conversion intensity in comparison to other materials, such as fluorides for example[34].

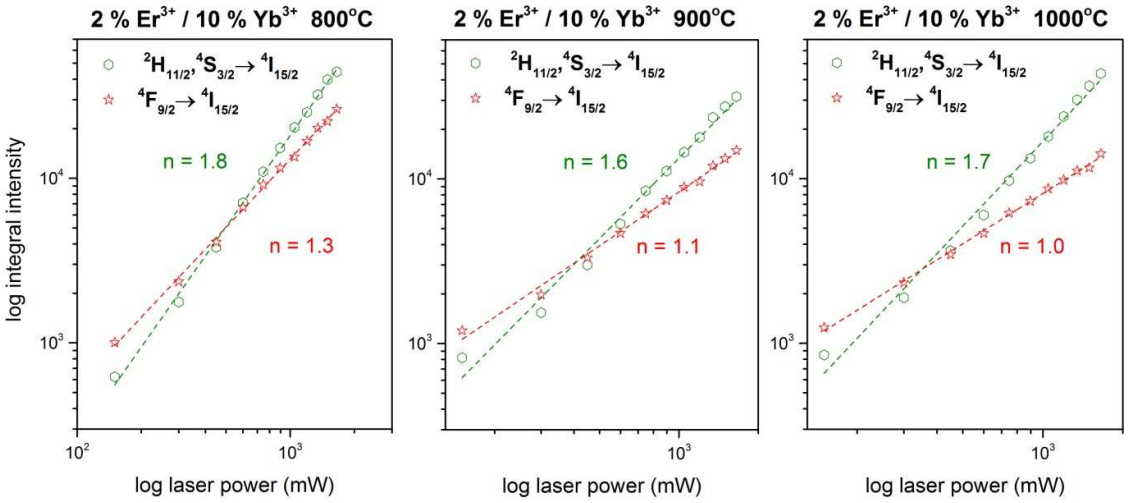

Fig. 12. Power dependence of the $Ca_{10}(PO_4)_6(OH)_2{\cdot}Ca_3(PO_4)_2$ composite doped with 2 mol% Er^{3+} and 10 mol% Yb^{3+} ions prepared at 800°C.

The pump power dependence of the green ($^2H_{11/2}$,$^4S_{3/2}$ → $^4I_{15/2}$) and red ($^4F_{9/2}$ → $^4I_{15/2}$) emissions were investigated (see Figure 12) as a function of sintering temperature for samples containing 2 mol% of Er^{3+} and 10 mol% of Yb^{3+} ions. The experimental results were fitted with linear function leading to the values of slopes of green band close to 2 and around 1 for red band, respectively confirming involvement of two photons in green emission. The situation was somewhat different in the case of the red emission. Actually, the $^4F_{9/2}$ level could be feed by at least three main processes (1) nonradiative decay from the $^2H_{11/2}$,$^4S_{3/2}$ levels, (2) through ETU involving the $^4I_{13/2}$ level and (3) cross relaxations II, III, and VI, respectively. As stated by Pollnau[41] if the nonradiative decay processes dominate both slopes of green and red emission tend to be close to 2. In the case, when the $^4F_{9/2}$ level is populated from $^4I_{15/2}$ through ETU slope of power dependence of the red band should be close to 3 (three photon process)[39]. In the studied case value of the power dependence of the $^4F_{9/2}$ →

$^4I_{15/2}$ transition was close to 1 pointing out on the increasing role of cross relaxation processes as similarly stated by Liu[42].

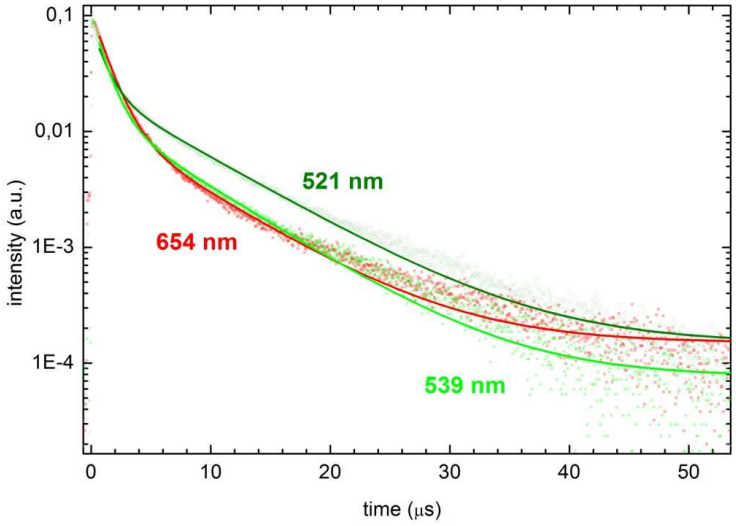

Fig. 13. Luminescence decays curves of the $Ca_{10}(PO_4)_6(OH)_2{\cdot}Ca_3(PO_4)_2$ nanocomposite doped with 2 mol% Er^{3+} and 10 mol% Yb^{3+} ions prepared at 800°C.

The luminescence decays were multiexponential and exhibited short and long decay components (Figure 13) equal to 1.44 ± 0.59 μs and 6.5 ± 2.3 μs for 654 nm, 1.48 ± 0.4 μs and 7.45 ± 0.3 μs for 521 and finally 1.8 ± 0.1 μs and 7.5 ± 1.0 μs at 539 nm. The double exponent behavior may be rationalized by two possible mechanisms. The first one could originate from surface effects. Therefore, Er^{3+} ions located within the aggregate core exhibit longer luminescence lifetimes, while those located at the surface are more susceptible to the local environment. As consequence they showed shorter luminescence lifetime. However, significant structural changes have been found as the annealing conditions were changed. While the sample annealed at 800°C shown significant contribution of β-TCP phase and differed from the samples annealed at higher temperatures, the elevation of annealing temperature, seems to increase the short decay component contribution as well as decrease of both short and long components of decay times (see Figure 14). It has to be mentioned that in classical examples of up-converting materials the radiative decay times of both green and red transitions in mixed metal oxides are usually of few hundred microseconds in a low concentrated samples. Fast both components especially upon comparison with bulk materials and lack of the visible rise times could imply presence of enhanced nonradiative transfers due to the presence of Er^{3+} surface rich regions and Er^{3+} - Er^{3+} ions at close distance due to the nano size character of particles in the former case and relatively high concentration of Er^{3+} in

the latter. It is well known that size reduction below micrometer results in detrimental effects reducing up-conversion intensity and efficiency[43,44].

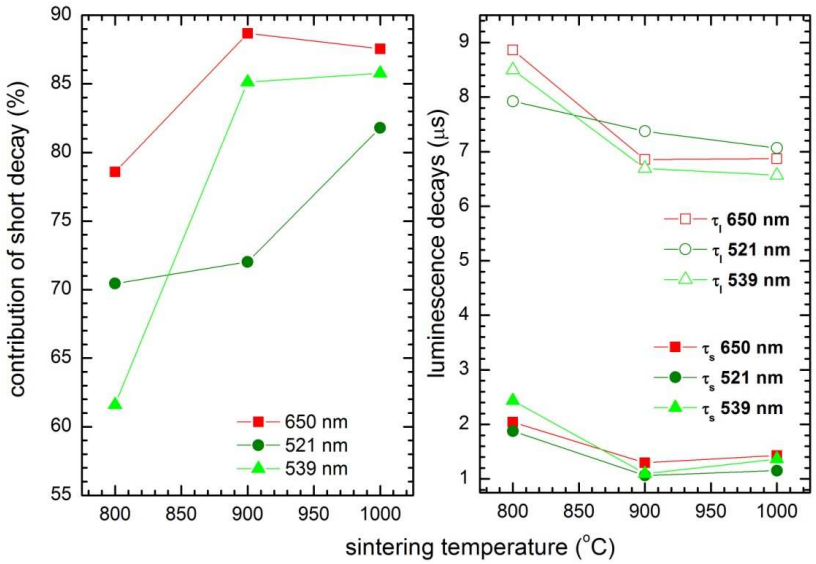

Fig. 14. Short decay component contribution (left) as well as values of short and long (c) decay components as a function of sintering temperature of the $Ca_{10}(PO_4)_6(OH)_2{\cdot}Ca_3(PO_4)_2$ nanocomposite doped with 2 mol% Er^{3+} and 10 mol% Yb^{3+}.

In the case of relatively high concentrated compounds it is expected that donor-donor energy transfer would be efficient leading to the concentration quenching effect[45]. In general energy was transferred to the traps and dissipated in crystalline net due to the overlap of *f* orbital wave functions of RE^{3+} through oxygen lattice band. Since, the Er^{3+} and Yb^{3+} were replacing Ca^{2+} ions in the $Ca_{10}(PO_4)_6(OH)_2{\cdot}Ca_3(PO_4)_2$ composite it was logically expected that it would induce formation of vacancies and enhance such nonradiative processes. Furthermore, one can clearly see that the decay time of the red emission was few times longer than green one. This might be a straightforward indication of a strong nonradiative CRs depopulating the green bands (as indicated in Figure 11).

The main aim of this section was to show the application prospects of developed system containing nanocomposite of the HAP@β-TCP optically activated with up-converting Er^{3+}/Yb^{3+} co-dopants. As it can be easily found in the literature biphasic HAP and TCP have shown very good osteoconductive potential[46] which is the main issue in bone tissue regeneration. However, we would like to propose to use different forms of nanocomposite HAP@β-TCP Er^{3+}/Yb^{3+} - lobes, pellets, tooth root filling material, or composite for covering titanium based implants (see Figures 15 and 16) and directly taking out of the advantages of this type of material in bio-related applications.

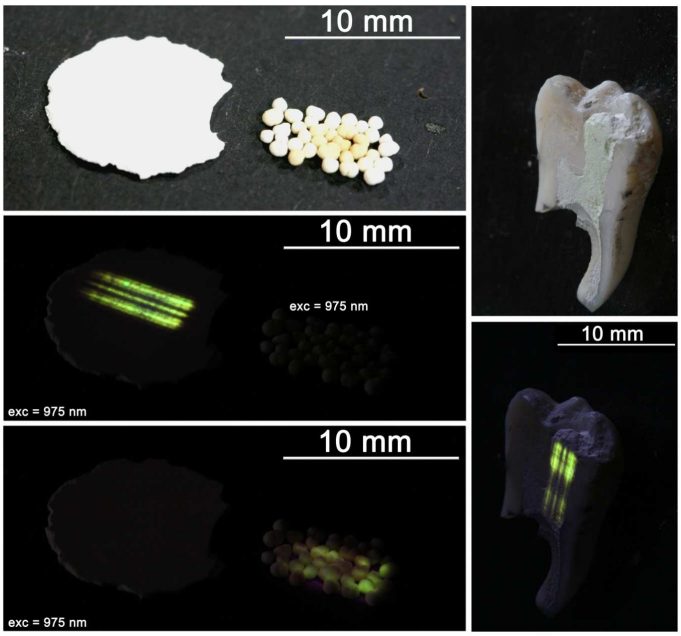

Fig. 15. Different forms of HAP@β-TCP Er^{3+}/Yb^{3+} up-converting nanocomposite, lobe and pellet (left part) tooth root filler (right) before and after excitation with NIR irradiation.

Application of the HAP@β-TCP Er^{3+}/Yb^{3+} lobes characterized by different size and thickness covered with collagen membranes could promote bone healing processes especially in the field of dental surgery and implantology.

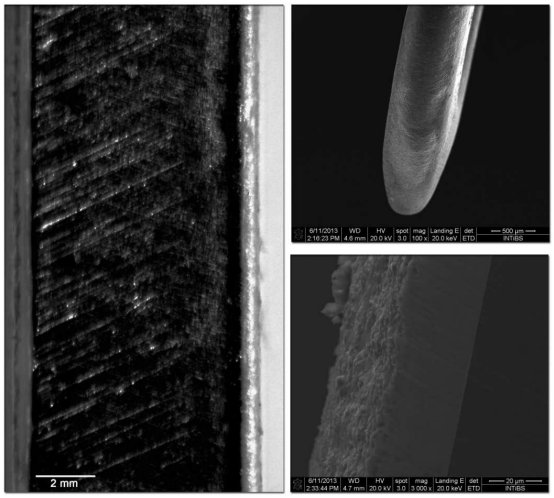

Fig. 16. Cross section of the titanium BOI implant covered with layer of HAP@β-TCP Er^{3+}/Yb^{3+} up-converting nanocomposite (left), side head view of the implant (upper right) and layer/implant boundary (bottom (right).

Pellets tailored to the specific size, with optimal porosity serving as carriers of antibiotics like for instance metronidazole could be used as bone substitute material in orthopedic and crano-facial surgery due to its high osteoconductive properties. Additional presence of the up-converting lanthanide cations might be utilized as bio-markers and specific indicators of bone

redevelopment as well as fate of the biomaterial in terms of its re-mineralization, re-absorption and presence of individual particles in place of application. The root filling HAP@β-TCP Er^{3+}/Yb^{3+} additionally loaded with antibiotics and steroids due to its biocompatibility could be used as a temporary or end filling materials especially when the lower pH at the inflammation side promotes release of Ca^{2+} ions from nanomaterials which is responsible for endothelium sealing and generation of phosphatase enzyme. Furthermore, the HAP@β-TCP activated with Er^{3+}/Yb^{3+} ions could be used for tooth labelling and studies of the remineralization or rebuilding of the dentin and/or enamel. Finally, the BOI type titanium implants could be easily covered with desired layer thickness to improve biocompatibility and bio integration with the bone tissue. As it can be seen the structure of the outer layer was porous and could be used for carrying the anti-inflammatory substances to minimize the risk of after-surgery complication or to speed up the healing process. Possibility of the bio-imaging of the HAP@β-TCP: Er^{3+}/Yb^{3+} outer layer might be useful in evaluation of the layer/implant ageing and to follow the integration of the implant with bone tissue by observation of the ion diffusion upon possible re-build of the boundary tissue. The colloids containing up-converting particles might be used in the IR-thermometry or for direct destruction of un-wanted cells utilizing thermal effects rising the particle temperature above 40°C already located at the specific destination place.

Conclusions

Up-converting HAP@β-TCP nanocomposites activated with Er^{3+}/Yb^{3+} ion-pairs were successfully fabricated using Pechini's technique with phase ratio being close to the 60:40 depending on the annealing conditions. The primary size of particles was evaluated by TEM 22 nm in the case of lowest thermal treatment whereas hydrodynamic size was around 220 nm and did not change significantly after time upon ATP stabilization. It has been shown that HAP@β-TCP modified with metronidazole could used as carrier for immediate drug release since there is only very weak bonding of metronidazole to the surface of proposed system. Cytotoxicity of nanocomposite was tested on canine osteosarcoma (D17) cells showing slight concentration dependent effect on cell viability whereas no effect was observed in the case of murine macrophage J774.E cells. It was found that the interplay of the intensity between transitions of the $^2H_{11/2} \rightarrow {}^4I_{15/2}$ and the $^4S_{3/2} \rightarrow {}^4I_{15/2}$ changes upon sample heating induced by different laser power giving a strong base for use of this material in emission thermometry. Analysis of the GRR ratio lead to the conclusions that increase of the GRR with laser power was attributed to the thermalization process resulting in higher population of the $^2H_{11/2} \rightarrow$

$^4I_{15/2}$. It was found that GRR depends strongly on the grain size of particles. The large particles contain lower fraction of optically active cations located close to surface areas, thus are less prone for non-radiative deactivation. The energy-level diagram was proposed for detailed description of up-conversion and accompanying process.

The recorded luminescence decays were multiexponential and exhibited short and long decay components with rather short values of decays in all cases. The double exponential behavior was rationalized by presence of surface effects meaning that Er^{3+} ions located within the aggregate core exhibit longer luminescence lifetimes, while those located at the surface are more susceptible to the local environment. Additionally relatively fast components of decay time as well as lack of rise times implies enhanced contribution of nonradiative transfers. This is mostly due to the presence of Er^{3+} surface rich regions due to the nano size character of particles. However existence of Er^{3+} - Er^{3+} ions at close distance because of relatively high concentration of Er^{3+} cannot be excluded as well. Therefore it is expected that donor-donor energy transfer would be efficient leading to the concentration quenching effect.

Acknowledgements

The authors would like to thank M.Sc. Ewa Bukowska for performing XRD measurements as well as Ph.D. Malgorzata Malecka for TEM images as well as M.Sc. Dorota Kida for pellets preparation. REGMED Clinic, Poland is gratefully acknowledged for donation of teeth. Financial support from the National Science Centre in course of realization of the Project 'Preparation and characterization of nanoapatites doped with rare earth ions and their biocomposites' no. UMO-2012/05/E/ST5/03904 is gratefully acknowledged.

References

[1] K. Rezwan, Q.Z. Chen, J.J. Blaker, A. R. Boccaccini, *Biomater.*, **2006**, *27*, 3413-3431.
[2] H. Liu, T.J. Webster, *Biomater.*, **2007**, *28*, 354-369.
[3] L.L. Hench and J. Wilson, *Sci.*, **1984**, *226*, 630-636.
[4] Z.Y. Li, W.M. Lam, C. Yang, B. Xu, G.X. Ni, S.A. Abbah, K.M.C. Cheung, K.D.K. Luk, W.W. Lu, *Biomater.*, **2007**, *28*, 1452-1460.
[5] O. Kozo, T. Yamamuro, T. Nakamura, T. Kokubo, *Biomater.*, **1990**, *11*, 265-271.
[6] D.K. Chatteriee, A.J. Rufalhah and Y. Zhang, *Biomater.*, **2008**, *29*, 937-943.
[7] S.A. Hilderbrand, F. Shao, Ch. Salthouse, U. Mahmood and R. Weissleder, *Chem. Comm.*, **2009**, *28*, 4188-4190.
[8] M.P. Ferraz, A.Y. Mateus, J.C. Sousa, F.J. Monteiro, *J. Biomed. Mater. Res. A*, **2007**, *81A*, 994-1004.
[9] E. Landi, A. Tampieri, G. Celotti, S. Sprio, M. Sandri, G. Logroscino, *Acta Biomater.*, **2007**, *3*, 961-969.
[10] I. Salma, G. Salms, M. Pilmane, D. Loca, J. Locs, N. Romanchikova, A. Skagers, L. Berzina Cimdina, Int. J. Oral Maxillofac. Surg., **2011**, *40*, 1216-1216.
[11] M.E. Fleet and Y.M. Pan, *J. Solid State Chem.*, **1994**, *112*, 78-87.
[12] L.D. DeLoach, S.A. Payne, L.L. Chase, L.K. Smith, W.L. Kway, W.F. Krupke, *IEEE J. Quantum Electr.*, **1993**, *29*, 1179-1191.
[13] K. Spariosu, R. D. Stultz, M. Birnbaum, T.H. Allik, J. A. Hutchinson, *Appl. Phys. Lett.*, **1993**, *62*, 2763-276.
[14] R. J. Wiglusz, A. Bednarkiewicz, A. Lukowiak, *Spectr. Lett.*, **2010**, *43*, 333-342.

[15] R. J. Wiglusz, A. Kedziora, A. Lukowiak, W.z Doroszkiewicz, W. Strek, *J. Biomed. Nanotechnol*., **2012**, *8*, 605-612.
[16] J. Rao, A. Dragulescu-Andrasi, H. Yao, *Curr. Opin. Biotechnol.*, **2007**, *18,* 17-25.
[17] Z. Li, Y. Zhang, S. Jiang, *Adv. Mater.*, **2008**, *20*, 4765-4769.
[18] Y. Zambito, E. Pedreschi, G. Di Colo, *Inter. J. Pharm.*, **2012**, *434,* 28-34.
[19] M. Yashima, A. Sakai, T. Kamiyama, and A. Hoshikawa, *J. Solid State Chem.*, **2003**, *175*, 272-277.
[20] E. Balan, S. Delattre, D.Roche, L. Segalen, G. Morin, M. Guillaumet, M. Blanchard, M. Lazzeri, Ch. Brouder, E. K. H. Salje, *Phys. Chem. Mineral.*, **2011**, *38*, 111–122.
[21] R.D. Shannon, *Acta Cryst.*, **1976**, ***A32***, 751-767.
[22] Y.C. Fung, Biomechanics. Mechanical Properties of Living Tissues, Springer-Verlag Inc., New York, 1993, 500.
[23] J.B. Park, Biomaterials Science and Engineering, Plenum Press, New York, 1987.
[24] H.M. Rietveld: *J. Appl. Cryst.* **1969**, *2*, 65-71.
[25] R. Delhez, T.H. de Keijser, J.I. Langford, D. Louër, E.J. Mittemeijer and E.J. Sonneveld, Crystal Imperfection Broadening and Peak Shape in the Rietveld Method, in: *The Rietveld Method*, edited by R.A. Young, Oxford Science, Oxford, United Kingdom (1993), 132.
[26] L. Luterotti and P. Scardi, *J. Appl. Cryst.,* **1990**, *23*, 246-252.
[27] L. Lutterotti, S. Matthies and H.-R. Wenk, *IUCr: Newsletter of the CPD*, **1999**, *21*, 14-15.
[28] V.R. Palkar, P. Ayyub, S. Chattopadhyay, M. Multani, *Phys. Rev. B*, **1996**, *53*, 2167-2170.
[29] R. Pązik, R. Anderson, L. Kępiński, V.G. Kessler, Gulaim A. Seisenbaeva, *J. Phys. Chem. C*, **2011**, *115*, 9850-9860.
[30] R.C. Murdock, L. Braydich-Stolle, A. M. Schrand, J.J. Schlager, S.M. Hussain, *Toxic. Sci.*, **2008**, *101*, 239-253.
[31] R.K. Singh, H.W. Kim, J Tissue Eng. Regen. Med., **2013**, *10*, 296-309.
[32] W. Tang, Y. Yuan, C. Liu, Y. Wu, X. Lu, J. Qian, *Nanomed.*, **2014**, *9,* 397-412.
[33] Y. Yuan, C. Liu, J. Qian, J. Wang, Y. Zhang, *Biomater*, **2010**, *31*, 730-740.
[34] H. Schafer, M. Hasse, *Angew. Chem. Int. Ed.,* **2011**, *50*, 5808-5829.
[35] M.L. Debasu, D. Ananias, I. Pastoriza-Santos, L.M. Liz-Marzan, J. Rocha, L.D. Carlos, *Adv. Mater.*, **2013**, *25*, 4868-4874
[36] T.V. Gavrilovic, D.J. Jovanovic, V. Lojpur, M.D. Dramicanin, *Sci. Rep.*, **2014**, *4*, 4209.
[37] B. Dong, S. Xu, J. Sun, S. Bi, D. Li, X. Bai, Y. Wang, L. Wang, *J. Mater. Chem.,* **2011**, *21*, 6193.
[38] K.W. Kramer, D. Biner, G. Frei, H.U. Gudel, M.P. Hehlen, S.R. Luthi, *Chem. Mater.,* **2004**, *18*, 1244-1251
[39] J.F. Suyver, J. Grimm, K.W. Kramer, H.U. Gudel, *J. Lumin*., **2005**, *114*, 53-59.
[40] F. Auzel, *Chem*. *Rev.*, **2004**, *104*, 139-173.
[41] M. Pollnau, D.R. Gamelin, S.R. Luthi, H.U. Gudel, *Phys. Rev. B,* **2000**, *61*, 3337-3346
[42] L. Liu, H. Jiang, Y. Chen, X. Zhang, Z. Zhang, Y. Wang, *J. Lumin.,* **2013**, *143*, 423-431.
[43] F. Auzel, D.C. Pecile, *R. Acad. Sci. Paris*, **1973**, *277B*, 155.
[44] J. Silver, M.I. Martinez-Rubio, T.G. Ireland, G.R. Fern, R.J. Withnall, *J. Phys. Chem*., **2001**, *B105*, 948.
[45] L. G. Van Uitert, R. C. Linares, R. R. Soden, A. A. Ballman, *J. Chem. Phys*., **1962**, *36*, 702.
[46] B.D. Boyan, Z. Schwartz, *Nat. Rev. Rheumatol.,* **2011**, *7*, 8-9.